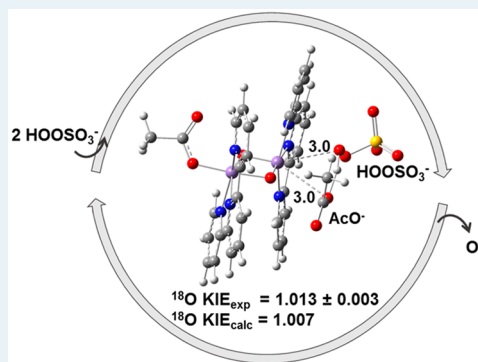


Mechanism of Manganese-Catalyzed Oxygen Evolution from Experimental and Theoretical Analyses of ^{18}O Kinetic Isotope EffectsSahr Khan,[†] Ke R. Yang,^{†,§} Mehmed Z. Ertem,^{†,§} Victor S. Batista,^{*,†} and Gary W. Brudvig^{*,†}[†]Department of Chemistry, Yale University, New Haven, Connecticut 06520-8107, United States[‡]Chemistry Department, Brookhaven National Laboratory, Building 555A, Upton, New York 11973, United States

S Supporting Information

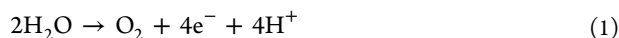
ABSTRACT: The biomimetic oxomanganese complex $[\text{Mn}^{\text{III/IV}}_2(\mu\text{-O})_2(\text{terpy})_2(\text{OH}_2)_2](\text{NO}_3)_3$ (**1**; terpy = 2,2':6',2''-terpyridine) catalyzes O_2 evolution from water when activated by oxidants, such as oxone ($2\text{KHSO}_5 \cdot \text{KHSO}_4 \cdot \text{K}_2\text{SO}_4$). The mechanism of this reaction has never been characterized, due to the fleeting nature of the intermediates. In the present study, we elucidate the underlying reaction mechanism through experimental and theoretical analyses of competitive kinetic oxygen isotope effects (KIEs) during catalytic turnover conditions. The experimental ^{18}O KIE is a sensitive probe of the highest transition state in the O_2 -evolution mechanism and provides a strict constraint for calculated mechanisms. The ^{18}O kinetic isotope effect of 1.013 ± 0.003 measured using natural abundance reactants is consistent with the calculated isotope effect of peroxymonosulfate binding to the complex, as described by density functional theory (DFT). This provides strong evidence for peroxymonosulfate binding being both the first irreversible and rate-determining step during turnover, in contrast to the previously held assumption that formation of a high-valent Mn-oxo/oxyl species is the highest barrier step that controls the rate of O_2 evolution by this complex. The comparison of the measured and calculated KIEs supplements previous kinetic studies, enabling us to describe the complete mechanism of O_2 evolution, starting from when the oxidant first binds to the manganese complex to when O_2 is released. The reported findings lay the groundwork for understanding O_2 evolution catalyzed by other biomimetic oxomanganese complexes, with features common to those of the O_2 -evolving complex of photosystem II, providing experimental and theoretical diagnostics of oxygen isotope effects that could reveal the nature of elusive reaction intermediates.

KEYWORDS: density functional theory, manganese complex, oxygen evolution mechanism, oxygen isotope effects, peroxymonosulfate



INTRODUCTION

The growing global energy demand and adverse environmental effects of fossil fuel usage have prompted the need for clean, carbon-neutral, and sustainable forms of energy.¹ Harnessing solar energy by the photochemical splitting of water into O_2 , electrons, and protons (eq 1) and then storing that energy in chemical bonds (solar fuels) is an attractive alternative to fossil fuels.^{2–5}



Nature, through billions of years of evolution, has provided us a blueprint for this difficult process in the form of photosynthesis.⁶ During photosynthesis, the multisubunit protein complex photosystem II (PSII), found in thylakoid membranes of all green plants, algae, and cyanobacteria, catalyzes the oxidation of water.^{7–10} The active site of PSII, called the O_2 -evolving complex (OEC), consists of an oxomanganese cuboidal structure, Mn_4CaO_5 , where metal centers (Mn and Ca) are linked by μ -oxo groups.¹¹ Because manganese is the metal of choice for Nature's water-splitting device,^{12,13} extensive research effort has been directed toward developing artificial water-oxidation catalysts based on oxomanganese complexes.^{14–18} A number of structural models of the OEC have been

synthesized,^{19–21} but achieving water-oxidation functionality with these models has been extremely challenging. The complex $[\text{Mn}^{\text{III/IV}}_2(\mu\text{-O})_2(\text{terpy})_2(\text{OH}_2)_2](\text{NO}_3)_3$ (**1**; terpy = 2,2':6',2''-terpyridine) is one of the few functional models of the OEC, which follows steady-state kinetics and evolves O_2 in the presence of chemical oxidants under homogeneous^{22–24} and heterogeneous^{25,26} conditions. Complex **1** has been extensively studied because of its high rate of O_2 evolution, the highest of any reported manganese-based O_2 -evolution catalyst to date.¹⁸ Several experimental techniques^{23,27–31} and computational methods^{32–36} have been applied to study the reactivity of this complex; however, the fast reaction rate and elusive nature of the reaction intermediates have made it difficult to determine the rate-limiting step and the catalytic mechanism. In fact, neither the nature of the catalyst functioning under turnover conditions nor the proposed intermediates could be actually confirmed. Here, we determine for the first time the actual catalytic species, the reaction intermediates, and the rate-determining step by using a combination of new experimental ^{18}O KIE data and computa-

Received: September 6, 2015

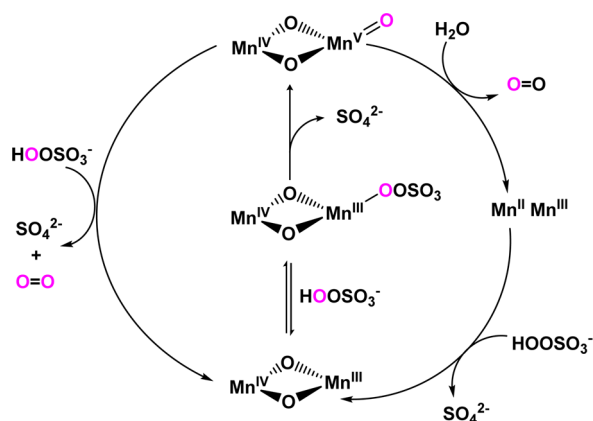
Revised: October 20, 2015

Published: October 22, 2015

tional modeling. We find that the rate-determining step involves ligand substitution, not formation of a high-valent Mn oxo intermediate or O–O bond formation as previously suggested. Furthermore, we find that the distal Mn(III) gets oxidized instead of the adjacent Mn(III) center, highlighting the essential role of charge transfer interactions mediated by the di- μ -oxo core. These findings provide a model for PSII for which there is growing evidence that O–O bond formation is not rate limiting.

There have been reports of efficient synthetic water-oxidation catalysts, including ruthenium complexes with turnover frequencies approaching that of the OEC,^{18,37} but accomplishing that level of performance with manganese complexes remains an outstanding challenge. Complex **1** achieves high O₂-evolution rates, but only in the presence of chemical oxidants, such as oxone (2KHSO₅·KHSO₄·K₂SO₄).²³ ¹⁸O isotopic-labeling studies have shown that, at moderate oxone concentrations of ~10 mM, one of the oxygen atoms of the evolved O₂ originates from the oxygen-transfer agent peroxymonosulfate while the other comes from the oxidation of water.^{23,28,38} The reaction with two peroxymonosulfate molecules to produce O₂ is the prevalent pathway at higher oxone concentration, while two oxygen atoms from water can be incorporated into O₂ under lower oxone concentration. During the course of the reaction, more oxygen atoms from water are incorporated in the evolved O₂ as the peroxymonosulfate concentration is depleted. These observations motivated previous studies to suggest the mechanism outlined in Scheme 1, where HSO₅[−] binds to Mn(III) to form a

Scheme 1. Previously Proposed Mechanism of O₂ Evolution Based on ¹⁸O-Labeling Studies^{a,23}



^aA truncated model of complex **1** is shown.

Mn^V=O intermediate, a species that might react with either H₂O or HSO₅[−] to liberate O₂. The Mn^V=O intermediate is proposed to slowly exchange with water, leading to the appearance of two water-derived oxygens in the evolved O₂. However, the actual nature of the reaction intermediates along the reaction mechanism remains to be established by detailed experimental and theoretical analysis, as addressed in this paper.

In the present study, we combine high-precision *natural abundance* competitive oxygen kinetic isotope effect (KIE) measurements and DFT calculations to examine the mechanism of O₂ evolution catalyzed by **1**. Competitive kinetic (*or equilibrium*) isotope effects arise when there is a change in isotopic composition of the transition state (*or products*) relative to the reactants.^{39,40} If the ¹⁸O KIE is greater than 1 (normal), ¹⁶O is more weakly bound in the transition state relative to the

reactant in comparison to ¹⁸O, and if it is less than 1 (inverse), then ¹⁶O is bonded more strongly. The O₂-evolution reaction mediated by **1** involves multiple bond-making and -breaking steps, and the size of the measured KIE, coupled with the theoretically determined isotope effects, can shed light on the irreversible and rate-limiting steps associated with catalysis.

We compare the ¹⁶O/¹⁸O ratio of the evolved O₂ (product) to the initial ¹⁶O/¹⁸O ratio of the peroxymonosulfate (reactant) under steady-state conditions and present a theoretical mechanism characterizing the dominant pathway of O₂ evolution catalyzed by **1** in the presence of peroxymonosulfate, a two-electron-donating oxygen-transfer agent.⁴¹ We find that, under turnover conditions, the binding of peroxymonosulfate to the Mn(IV) center is the rate-limiting and first irreversible step, a process that determines the competitive ¹⁶O/¹⁸O kinetic isotope effect. In contrast to the previously proposed mechanism, where the O–O bond cleavage upon peroxymonosulfate binding to the Mn(III) center leads to the formation of a reactive Mn^V=O intermediate, our results suggest that a Mn^{IV}–O• intermediate is formed through O–O bond cleavage upon peroxymonosulfate binding to the Mn(IV), a process that oxidizes the distal Mn(III) center through an intramolecular electron-transfer reaction mediated by the di- μ -oxo–di-Mn core. These findings provide a fundamental understanding that should be valuable for the design of better water-oxidation catalysts and for understanding common mechanistic aspects of water oxidation catalyzed by the OEC of PSII.

RESULTS

Experimental ¹⁶O/¹⁸O Kinetic Isotope Effect. The experimental KIE of 1.013 ± 0.003 was measured by comparing the ¹⁸O content of the O₂ evolved to the initial isotopic composition of peroxymonosulfate. The isotopic compositions of the buffer solution, oxone, and evolved O₂ were determined by isotope ratio mass spectrometry, a technique that measures isotope ratios to a precision of ±0.0001.⁴² A helium-saturated mixture of complex **1** and oxone in a buffer solution reacted for different lengths of time (ranging from 15 s to 5 min) to cause different fractional conversions of oxone. The O₂ evolved was purified and collected in molecular sieves using a home-built vacuum apparatus. The O₂ gas was then directly analyzed on a dual-inlet mass spectrometer at the Earth Systems Center for Stable Isotopic Studies, Yale University. The ¹⁶O/¹⁸O ratio of the buffer solution (0.23 M HOAc/OAc[−], pH 4.5) was determined by carbon dioxide equilibration using a Gas-Bench setup.⁴³ We have previously shown by Raman spectroscopy and mass spectrometry that the oxygen atoms in oxone do not exchange with water;²³ therefore, the ¹⁸O content of oxone was determined separately. Oxone exists as a triple salt with multiple oxygen atoms; however, only the peroxo oxygen in peroxymonosulfate (HOOSO₃[−]) is reactive. The peroxo oxygen was extracted into pure triphenylphosphine to form triphenylphosphine oxide.⁴⁴ The sample oxide was then pyrolyzed at 1450 °C in a carbon reducing environment, and its oxygen isotopes were measured using a Thermal Conversion Elemental Analyzer connected to a mass spectrometer.⁴⁵

Figure 1 shows the isotope fractionation plot of the O₂ evolved catalytically by 1250 μM of complex **1** in 600 mM oxone solution. The competitive KIE was calculated using the Rayleigh equation:⁴⁶

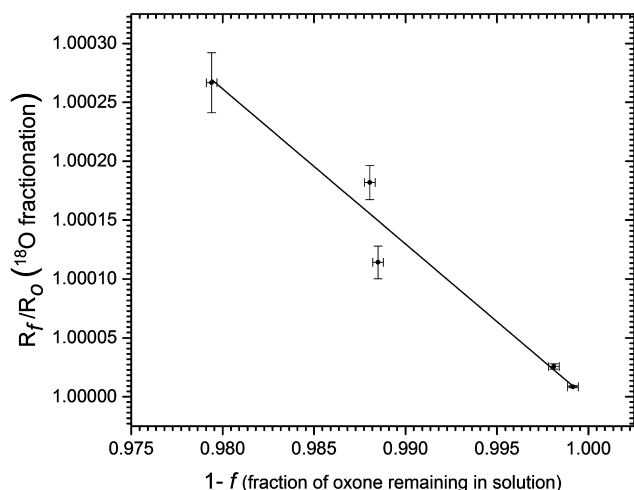


Figure 1. Isotope fractionation of O_2 evolution catalyzed by complex **1** under high oxone concentration plotted on natural logarithm (ln) scales. All of the data points are shown with error bars representing standard errors.

$$\text{KIE} = \left[1 + \frac{\ln(R_f/R_0)}{\ln(1-f)} \right]^{-1} \quad (2)$$

where R_0 is the initial $^{16}\text{O}/^{18}\text{O}$ ratio of oxone before adding **1** and R_f is the final oxone $^{16}\text{O}/^{18}\text{O}$ ratio at fractional consumption, f .

Determination of the Extent of Oxone and Water Reaction Pathways. Labeling studies have shown that, under moderate or low oxone concentration, one of the oxygen atoms of the evolved O_2 originates from water and that the incorporation of oxygen from water increases with time as oxone is consumed.^{23,28,38} We ran our experiments for a low number of turnovers under high oxone concentration to minimize the incorporation of water oxygen atoms and simplify the isotope analysis. Under these conditions, the measured ^{18}O fractionation is dependent only on the intrinsic KIE of the first irreversible step of the mechanism and not on the differential incorporation of ^{18}O atoms from two different sources. Additionally, the short reaction time minimizes the effect of catalyst deactivation. We find that low turnover numbers render oxygen fractionation difficult to measure; therefore, extreme care was taken to precisely determine the experimental isotope effect by multiple repetitions and by performing the study in a custom-designed microanalytical vacuum setup.

The determined ^{18}O KIE assumes that peroxymonosulfate is the only reactant and that there is no effect of H_2^{18}O on the measurement. This was scrutinized by running the reaction in slightly ^{18}O enriched water (still at natural abundance). Table 1 shows that the isotopic composition of solvent water has little effect on the $^{16}\text{O}/^{18}\text{O}$ ratio of the evolved O_2 , even at the highest

Table 1. Comparison of the Isotopic Composition of O_2 Evolved in Deionized and Slightly ^{18}O Enriched Water (Both Natural Abundance) at the Highest Fractional Consumption, f , Used for Calculation of the ^{18}O KIE

sample	^{18}O atomic percentage
deionized water	0.199425 ± 0.000005
catalytic O_2 evolved in deionized water	0.2023 ± 0.0002
slightly ^{18}O enriched water	0.201855 ± 0.00005
catalytic O_2 evolved in slightly ^{18}O enriched water	0.2029 ± 0.0003

fractional consumption, f , used for the KIE calculation, showing that under high concentration of oxone and low turnover numbers virtually all of the O_2 produced comes from oxone.

Computational Investigation of the Reaction Mechanism. We performed density functional theory (DFT) calculations, based on the B3LYP functional,^{47,48} with 15% Hartree–Fock exchange and dispersion correction in conjunction with the PCM aqueous continuum solvation model⁴⁹ to characterize the reaction intermediates along the mechanism shown in Schemes 2 and 3. Dispersion effects were considered by adding Grimme's D2 version of dispersion correction,⁵⁰ denoted as B3LYP-D2. For comparison, we also performed calculations based on the M06-L⁵¹ functional, as discussed in the Supporting Information. ^{18}O equilibrium isotope effects (EIEs) and kinetic isotope effects (KIEs) were calculated for each of the reaction steps, using the vibrational frequencies obtained at the B3LYP-D2 level of theory and the transition-state theory formalism, as implemented in recent applications.^{52,53} The EIEs were computed as ratios of molecular partition functions for reactants and products with ^{18}O and ^{16}O , obtained from the vibrational frequencies of reactants and products ν_i^{R} and ν_j^{P} , respectively, as follows:

$$^{18}\text{O EIE} = \frac{\prod_j^{3N-6} \frac{\exp(h\nu_j^{\text{P}(^{18}\text{O})} / 2kT)}{\exp(h\nu_j^{\text{P}(^{16}\text{O})} / 2kT)}}{\prod_i^{3N-6} \frac{\exp(h\nu_i^{\text{R}(^{18}\text{O})} / kT)}{\exp(h\nu_i^{\text{R}(^{16}\text{O})} / kT)}} \times \frac{\prod_j^{3N-6} \frac{1 - \exp(-h\nu_j^{\text{P}(^{18}\text{O})} / kT)}{1 - \exp(-h\nu_j^{\text{P}(^{16}\text{O})} / kT)}}{\prod_i^{3N-6} \frac{1 - \exp(-h\nu_i^{\text{R}(^{18}\text{O})} / 2kT)}{1 - \exp(-h\nu_i^{\text{R}(^{16}\text{O})} / 2kT)}} \times \frac{\prod_j^{3N-6} \frac{\nu_j^{\text{P}(^{16}\text{O})}}{\nu_j^{\text{P}(^{18}\text{O})}}}{\prod_i^{3N-6} \frac{\nu_i^{\text{R}(^{16}\text{O})}}{\nu_i^{\text{R}(^{18}\text{O})}}} \quad (3)$$

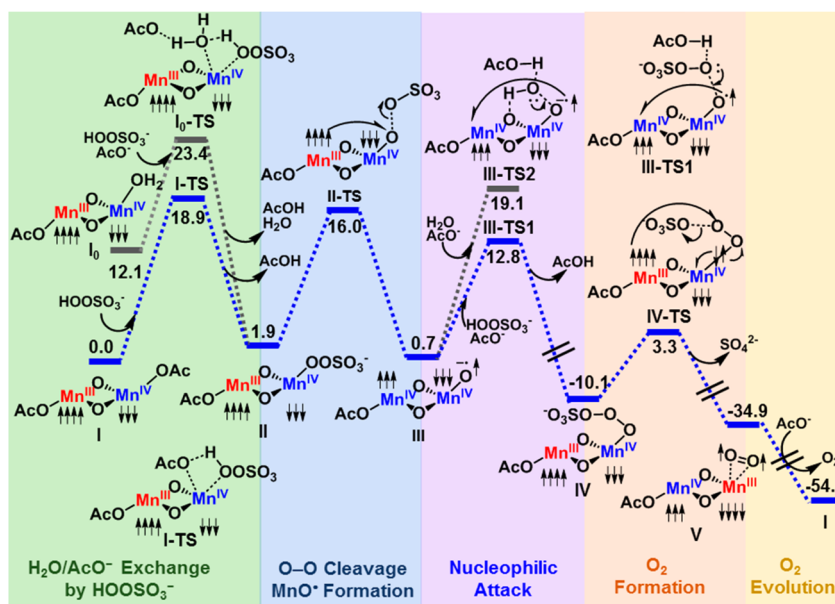
where the three terms in eq 3 correspond to the usual isotope effects on the zero point energy (ZPE), the vibrational excitation energy (EXC), and the mass and moments of inertia (MMI). In eq 3, k and T are the Boltzmann constant and absolute temperature, respectively. The ^{18}O KIEs were calculated analogously from the molecular partition functions of reactants and transition states, as follows:

$$^{18}\text{O KIE} = \nu_{\text{RC}}^{18} \times \frac{\prod_j^{3N-7} \frac{\exp(h\nu_j^{\text{TS}(^{18}\text{O})} / 2kT)}{\exp(h\nu_j^{\text{TS}(^{16}\text{O})} / 2kT)}}{\prod_i^{3N-6} \frac{\exp(h\nu_i^{\text{R}(^{18}\text{O})} / kT)}{\exp(h\nu_i^{\text{R}(^{16}\text{O})} / kT)}} \times \frac{\prod_j^{3N-7} \frac{1 - \exp(-h\nu_j^{\text{TS}(^{18}\text{O})} / kT)}{1 - \exp(-h\nu_j^{\text{TS}(^{16}\text{O})} / kT)}}{\prod_i^{3N-6} \frac{1 - \exp(-h\nu_i^{\text{R}(^{18}\text{O})} / 2kT)}{1 - \exp(-h\nu_i^{\text{R}(^{16}\text{O})} / 2kT)}} \times \frac{\prod_j^{3N-7} \frac{\nu_j^{\text{TS}(^{16}\text{O})}}{\nu_j^{\text{TS}(^{18}\text{O})}}}{\prod_i^{3N-6} \frac{\nu_i^{\text{R}(^{16}\text{O})}}{\nu_i^{\text{R}(^{18}\text{O})}}} \quad (4)$$

where ν_{RC}^{18} is the ratio of the imaginary frequencies of the transition states associated with light (e.g., ^{16}O) and heavy (e.g., ^{18}O) isotopologues (see the Supporting Information) and the remaining three terms are similar to the three terms in eq 3. Multiple mechanisms were calculated and analyzed (see the Supporting Information for details), with the reaction pathway shown in Schemes 2 and 3 found to be the most consistent with the experimental values of KIEs and observed saturation kinetics.

Complex **1** exchanges a water ligand with AcO^- when it is dissolved in the acetate buffer solution, as shown by electro-

Scheme 2. Reaction Mechanism of O₂ Evolution Due to Activation of the Precatalyst [(AcO)Mn^{III}(μ-O)₂Mn^{IV}(OH₂)(terpy)₂]²⁺ and the Active Catalyst [(AcO)Mn^{III}(μ-O)₂Mn^{IV}(OAc)(terpy)₂]⁺ by Peroxymonosulfate as a Primary Oxidant^a



^aEnergies are indicated in kcal/mol as obtained at the DFT B3LYP15-D2 level of theory. Up and down arrows indicate the unpaired α and β electrons. The manganese complex is shown sans the terpy ligands.

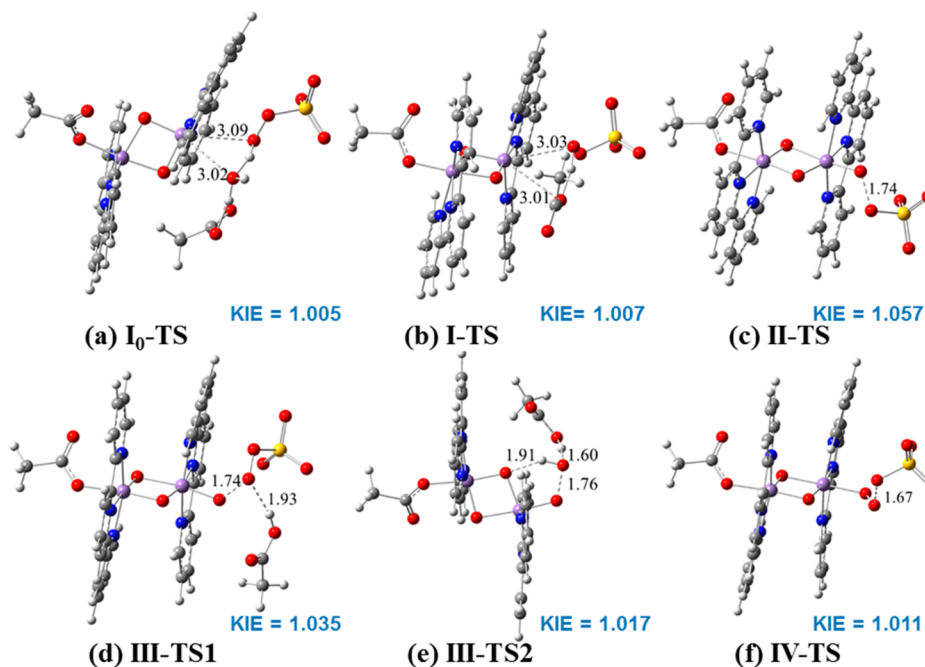


Figure 2. Optimized transition-state structures for (a) water exchanged by HSO₅[−] (I₀-TS), (b) acetate exchanged by HSO₅[−] (I-TS), (c) O–O bond scission to generate the reactive Mn^{IV}–O• intermediate (II-TS), O–O bond formation by nucleophilic attack by (d) HSO₅[−] (III-TS1), or (e) H₂O (III-TS2), and (f) O₂ evolution (IV-TS). Key bond lengths are shown in Å.

chemical titrations,³¹ mass spectrometry,²⁸ two-dimensional hyperfine sublevel correlation spectroscopy (HYSCORE),⁵⁴ and DFT calculations.^{33,35} Our calculations show that the free energy barriers for exchange of water by acetate bound to Mn(III) and Mn(IV) are 13.3 and 20.2 kcal/mol (see Scheme S4 in the Supporting Information), indicating that the water bound to Mn(III) exchanges quickly with acetate and forms [(AcO)Mn^{III}(μ-O)₂Mn^{IV}(OH₂)(terpy)₂]²⁺, as suggested by HYSCORE.⁵⁴ However, [(AcO)Mn^{IV}(μ-O)₂Mn^{III}(OH₂)(terpy)₂]²⁺

is slightly more stable than [(AcO)Mn^{III}(μ-O)₂Mn^{IV}(OH₂)(terpy)₂]²⁺ and both species are predicted to be found at equilibrium. Therefore, we explored the reactivity of both of these complexes and formation of the Mn^{IV}–O• intermediate, as shown in the Supporting Information. However, during multiple turnovers, the ligand exchange of triplet O₂ generated at the complex with acetate is more relevant. The O₂ released makes way for the AcO[−] to bind at Mn(III) to generate [(AcO)Mn^{IV}(μ-O)₂Mn^{III}(OAc)(terpy)₂]⁺, the active catalyst, which is thermo-

dynamically more stable than both $[(\text{AcO})\text{Mn}^{\text{IV}}(\mu\text{-O})_2\text{Mn}^{\text{III}}(\text{OH}_2)(\text{terpy})_2]^{2+}$ and $[(\text{AcO})\text{Mn}^{\text{III}}(\mu\text{-O})_2\text{Mn}^{\text{IV}}(\text{OH}_2)(\text{terpy})_2]^{2+}$. This is consistent with the experimental observation of the diacetate complex by electrospray ionization mass spectrometry (ESI-MS) under turnover conditions.²⁸

Scheme 2 shows the mechanism of reaction of the precatalyst $[(\text{AcO})\text{Mn}^{\text{III}}(\mu\text{-O})_2\text{Mn}^{\text{IV}}(\text{OH}_2)(\text{terpy})_2]^{2+}$ (**I**₀) (one-turnover conditions) and the active catalyst $[(\text{AcO})\text{Mn}^{\text{III}}(\mu\text{-O})_2\text{Mn}^{\text{IV}}(\text{OAc})(\text{terpy})_2]^+$ (**I**) (multiple-turnover conditions) with HSO_5^- . The first step involves exchange of H_2O or AcO^- by HSO_5^- to form $[(\text{AcO})\text{Mn}^{\text{III}}(\mu\text{-O})_2\text{Mn}^{\text{IV}}(\text{SO}_5)(\text{terpy})_2]$ (**II**). **I**₀ reacts with a forward barrier of 11.3 kcal/mol, while **I** has a barrier of 18.9 kcal/mol. The calculated $^{16}\text{O}/^{18}\text{O}$ KIEs associated with these reactions are 1.005 and 1.007, both comparable to the measured value of 1.013 ± 0.003 , but only the ΔG^\ddagger value of the reaction of **I** with HSO_5^- matches the experimentally observed KIE and saturation kinetics as described below. As shown in **Figure 2b**, the transition state (TS) corresponding to the substitution of AcO^- by HOOSO_3^- can be classified as a dissociative TS, since the Mn–O distances between the leaving AcO^- and incoming HOOSO_3^- , are 3.01 and 3.03 Å, respectively, which is a result of the steric repulsion around the Mn(IV) center. In the transition state (**I**-TS), the anionic AcO^- is dissociated from the positive Mn(IV) center, while the bond between the incoming HOOSO_3^- and the Mn(IV) center is not formed yet. Thus, a large barrier is associated with the initial ligand substitution. After the transition state is passed, the proton in HOOSO_3^- transfers to AcO^- to release AcOH . The observation of slow exchange of ligands in complexes containing Mn(IV) is not surprising, as reviewed by Vinyard et al.;¹⁰ however, in this investigation we have shown that the exchange of anions associating with the Mn complex (acetate replaced by peroxymonosulfate) is slower than an O–O cleavage step. The sterics and electrostatics associated with this ligand substitution increases the barrier of the transition state, making it rate limiting during catalysis.

The SO_5^{2-} bound in intermediate **II** undergoes O–O bond scission (**II**-TS) to yield the reactive $\text{Mn}^{\text{IV}}\text{-O}^\bullet$ oxyl-radical intermediate (**III**). This $2e^-$ oxidation step proceeds with $\Delta G^\ddagger = 14.1$ kcal/mol and has a large intrinsic kinetic isotope effect, $\text{KIE}_2 = 1.057$, similar to those reported for other O–O bond-cleavage reactions.⁵⁵ In contrast to the previously proposed mechanism (**Scheme 1**), DFT predicts that the di- μ -oxo bridge mediates intramolecular electron transfer and the Mn center oxidized by oxone is the distal Mn (rather than the Mn center where HSO_5^- initially binds), generating the resulting oxyl-radical species. This finding highlights the importance of the di- μ -oxo–di-Mn core, suggesting that a similar functional role might be found for the di- μ -oxo bridges of the OEC in PSII.

The $\text{Mn}^{\text{IV}}\text{-O}^\bullet$ intermediate, with the unpaired electron on O antiparallel to the three β electrons on the adjacent Mn(IV) center, undergoes nucleophilic attack by either HSO_5^- or H_2O to form the O–O bond, a process assisted by AcO^- functioning as a proton acceptor.³⁶ The attack by peroxymonosulfate has a lower activation free energy barrier ($\Delta G^\ddagger = 12.1$ kcal/mol) than the nucleophilic attack by H_2O , which has the activation free energy barrier $\Delta G^\ddagger = 18.4$ kcal/mol. The intrinsic KIE_3 s for the nucleophilic attack by peroxymonosulfate and H_2O are 1.035 and 1.017, respectively, consistent with the ^{18}O KIEs reported for similar reactions in other systems.^{52,53,56} The barrier for the water-nucleophilic attack is higher than that for peroxymono-

sulfate, in agreement with the experimental observation that water reacts only under a low concentration of oxone.

The nucleophilic attack of peroxymonosulfate on the $\text{Mn}^{\text{IV}}\text{-O}^\bullet$ oxyl-radical species **III** generates the complex $[(\text{AcO})\text{Mn}^{\text{III}}(\mu\text{-O})_2\text{Mn}^{\text{IV}}(\text{OOOSO}_3)(\text{terpy})_2]$ (**IV**) with both Mn centers in low-energy high-spin states (quartet for Mn^{IV} and quintet for Mn^{III}), where the distal Mn center is reduced to Mn^{III} . The di- μ -oxo bridge is critical to mediate the intramolecular electron transfer responsible for reduction of the distal Mn center. The geometries of optimized transition states and the associated ^{18}O KIEs are shown in **Figure 2**. Interestingly, the O–O bond lengths in both O–O scission (**II**-TS and **IV**-TS) and O–O formation (**III**-TS1 and **III**-TS2) reactions are around 1.7 Å. The transition states of O–O bond formation, formed by acetate-assisted nucleophilic attack by either HSO_5^- (**III**-TS1) or H_2O (**III**-TS2), involve proton transfer to acetate.

The $[(\text{AcO})\text{Mn}^{\text{III}}(\mu\text{-O})_2\text{Mn}^{\text{IV}}(\text{OOOSO}_3)(\text{terpy})_2]$ complex undergoes O–O bond cleavage to release SO_4^{2-} and form the triplet O_2 bound complex $[(\text{AcO})\text{Mn}^{\text{IV}}(\mu\text{-O})_2\text{Mn}^{\text{III}}(^3\text{O}_2)(\text{terpy})_2]^{2+}$ (**V**) with an activation barrier of 13.4 kcal/mol. The distal Mn center is oxidized to Mn^{IV} , and the adjacent Mn center becomes Mn^{III} . We note that, after one turn of the catalytic cycle, the Mn center adjacent to AcO^- becomes Mn^{IV} . The weakly bound triplet O_2 is replaced by AcO^- , generating the catalytic starting species $[(\text{AcO})\text{Mn}^{\text{IV}}(\mu\text{-O})_2\text{Mn}^{\text{III}}(\text{OAc})(\text{terpy})_2]^+$ (**I**).

Experimental and Theoretical Deuterium Isotope Effects. The noncompetitive ^2H KIE of complex **1** under high oxone conditions was determined by comparing the initial rates of O_2 evolution by **1** in deuterated and undeuterated buffers (**Table 2**). The ^2H KIE of 0.99 ± 0.07 measured in this study

Table 2. ^2H Isotope Effect on the O_2 -Evolution Reaction of Complex **1** with Different $[\text{HSO}_5^-]_{\text{initial}}:[\text{1}]_{\text{initial}}$ Mole Ratios

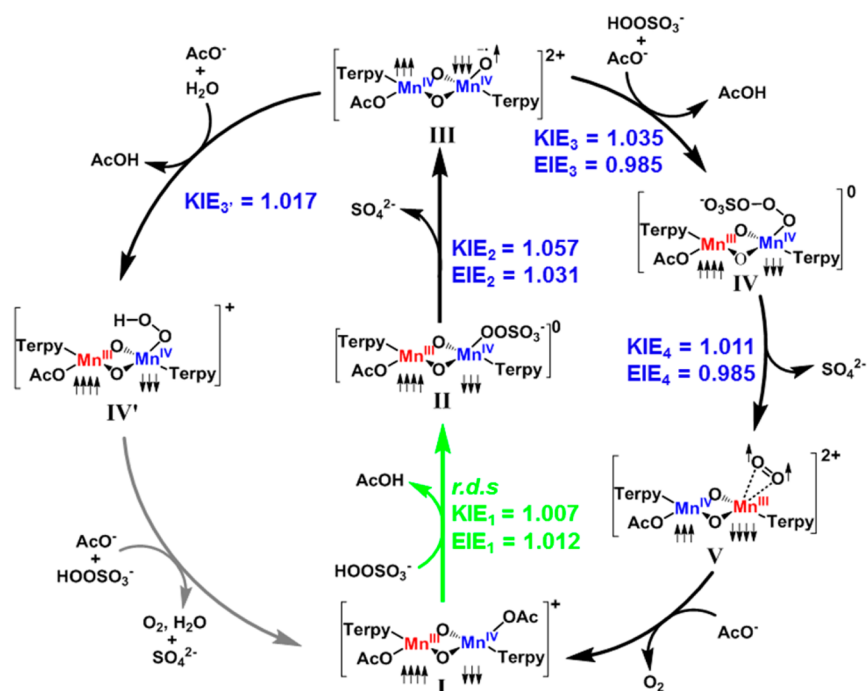
$[\text{HSO}_5^-]:[\text{1}]$	^2H isotope effect	ref
20:1	1.71 ± 0.2	20
100:1	1.64 ± 0.02	20
500:1	0.99 ± 0.07	this work

when the ratio of oxone to complex **1** is 500:1 is smaller than those determined in previous studies under lower oxone concentrations.²³ The DFT calculated deuterium isotope effect of the highest barrier step (binding of HSO_5^-) in **Scheme 2** is 1.28 (**I**-TS), which is compatible with the experimentally observed value.^{57,58}

DISCUSSION

The measured competitive *natural abundance* ^{18}O KIE of 1.013 ± 0.003 represents the isotope effect on $k_{\text{cat}}/K_{\text{M}}$ (or V/K) and encompasses all the steps from when peroxymonosulfate first interacts with complex **1**, up to and including the transition state of the first irreversible (usually rate-determining) step of the catalytic reaction.^{42,46,59} If the rate-limiting step corresponds to the first irreversible step, then the KIE on $k_{\text{cat}}/K_{\text{M}}$ is fully expressed in the measured fractionation and there is no contribution of the EIEs preceding the rate-determining step. For reactions in which there are multiple partial rate-limiting steps, the overall KIE is calculated as a weighted average of the intrinsic KIEs corresponding to those steps.^{60,61} The combined experimental and theoretical KIEs have enabled us to postulate a detailed and complete mechanism of O_2 evolution catalyzed by complex **1**, which is summarized in **Scheme 3**.

Scheme 3. Complete Catalytic Cycle of O₂ Evolution from the Active Catalyst I upon Activation by Peroxymonosulfate (HOOSO₃[−]) in an Acetate Buffer under Turnover Conditions^a



^aThe reaction steps shown in black are studied in detail in the present study. Intrinsic ¹⁸O kinetic isotope effect (KIE) and equilibrium isotope effect (EIE) factors obtained with B3LYP-D2 are indicated in blue. The calculated rate-determining step is labelled with *r.d.s.* and is highlighted in green.

The measured ¹⁸O KIE of 1.013 ± 0.003 and the calculated ¹⁸O KIE₁ of 1.007 corresponding to binding of HSO₅[−] to **I** agree well with one another, providing strong evidence that initial ligand substitution is the first irreversible step during catalysis. The calculated free energy of activation of substitution of AcO[−] by HSO₅[−] (ΔG[‡] = 18.9 kcal/mol) is in agreement with the 15.4 kcal/mol value estimated using transition state theory from the experimental *V*_{max} value of the reaction of **1** with oxone.^{23,28}

The free energy diagram for the proposed reaction mechanism in Scheme 2 indicates that the free energy of activation values for O–O bond scission (ΔG[‡] = 14.1 kcal/mol), O–O bond formation (ΔG[‡] = 12.1 kcal/mol), and O₂ release (ΔG[‡] = 13.5 kcal/mol) are smaller than that of peroxymonosulfate binding (ΔG[‡] = 18.9 kcal/mol). We had previously proposed the formation of Mn^{IV}–O• as the rate-determining step in the reaction of **1** with peroxymonosulfate (Scheme 1);²³ however, the DFT results summarized in Scheme 3 show that the calculated KIE₂ (1.057) is significantly higher than the observed experimental KIE, indicating that the O–O bond cleavage could not be the observed isotope-sensitive step. This further supports the conclusion that **I**₀ is not the active catalyst, because the measured ¹⁸O KIE, a composite of the calculated KIEs associated with both ligand substitution and O–O bond cleavage (the rate-determining step), would be much larger than 1.013. The calculated KIE₄ (1.011) of the triplet O₂ formation step alone could be comparable to the experimentally measured ¹⁸O KIE, but since the observed fractionation measures all steps beginning with the peroxymonosulfate encounter to the first irreversible step, the overall calculated KIE comes out to be very large (~1.039), as all the EIEs preceding the irreversible step should be accounted for to obtain the overall KIE. The KIEs and calculated activation free energies suggest that the reaction intermediates **II**–**V** would be very short lived, which is consistent with the fact

that no oxidized intermediate species in the catalytic reaction of **1** with peroxymonosulfate have been experimentally observed.^{28,30}

We also studied the O₂-evolution mechanism starting with different initial reactants ([(H₂O)Mn^{III}(μ-O)₂Mn^{IV}(OAc)(terpy)₂]²⁺ and [(AcO)Mn^{III}(μ-O)₂Mn^{IV}(OH₂)(terpy)₂]²⁺) and at different level of theories, and those results are available in the Supporting Information. One consistent theme for all the plausible alternative mechanisms is initial binding of HSO₅[−] being the first irreversible step so that the fractionation of oxygen occurs at the initial ligand substitution step (see the Supporting Information for details). Slow ligand displacement reactions (e.g., anation) are commonly observed in ruthenium water-oxidation catalysts such as the blue dimer.⁶² However, our study represents perhaps the first report of ligand exchange being irreversible and rate determining in a manganese O₂-evolution catalyst.

Under low oxone concentration, H₂O could also perform a nucleophilic attack on the Mn^{IV}–O• moiety (Scheme 2). This is manifested in the ²H isotope effect measurements for the reaction with different peroxymonosulfate concentrations, as shown in Table 2. The calculated primary deuterium isotope effect for the proposed rate-determining step (**I**-TS) is small (1.28), in agreement with the experimental observations. The measured deuterium isotope effects have a larger intrinsic error because, unlike ¹⁸O KIE, they could have contributions from both primary and secondary ²H isotope effects, but the absence of a large primary calculated deuterium isotope effect on the predicted rate-determining step lends further support to the ¹⁸O KIE study. The measured ²H isotope effect increases with decreasing initial concentrations of oxone, as water becomes more involved in the reaction, indicating that both oxidant binding (ΔG[‡] = 18.9 kcal/mol) and water nucleophilic attack

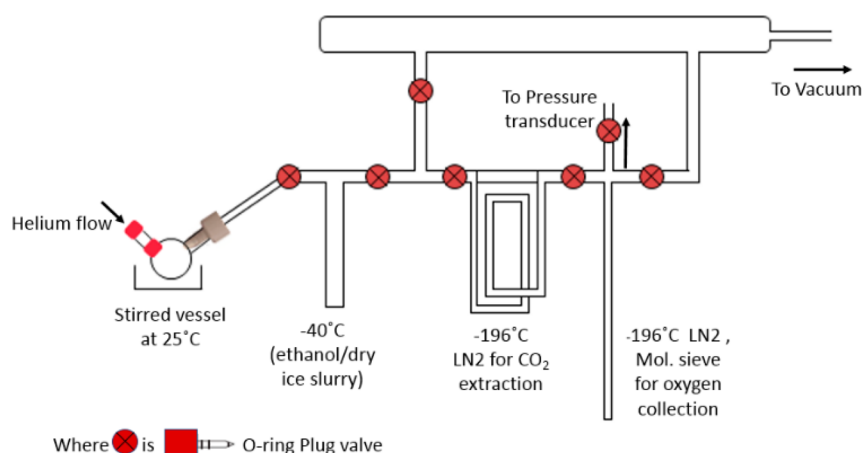


Figure 3. Schematic of the vacuum setup for oxygen isotope experiments. The reaction chamber (stirred and at 25 °C) is connected to an outer chamber filled with helium via a septum. The solutions are injected through the outer chamber through BTO septa to prevent any air leaks upon catalyst injection into the reaction chamber. The other side of the reaction chamber is connected to the vacuum line, which is equipped with a water trap (−40 °C with ethanol/dry ice), CO₂ trap (−196 °C with liquid nitrogen), and the collection tubes with 5 Å molecular sieves (−196 °C with liquid nitrogen). Not shown in the schematic is the molecular sieves preparation tube maintained at 300 °C with a furnace.

($\Delta G^\ddagger = 18.4$ kcal/mol) are becoming partially rate limiting and contributing to the ²H KIE.

CONCLUSIONS

In summary, we present the complete reaction mechanism of O₂ evolution by **1** activated by peroxyxymonosulfate as the primary oxidant, supported by the combined experimental and theoretical study of competitive ¹⁸O kinetic isotope effects. This study provides a detailed theoretical outlook on the action of chemical oxidants on O₂-evolution catalysts, an area that has not been well explored. We find that the first irreversible step involves substrate binding to **1**, which is a novel observation for a manganese O₂-evolving catalyst. After this step, the succeeding steps leading to O₂ evolution are fast due to their low activation free energies. This described mechanism is consistent with and helps explain previously published steady-state kinetics,²³ electron paramagnetic resonance,²⁸ ¹⁸O labeling,^{23,27,28} and electrochemical³¹ studies done on **1**.

The experimental and calculated KIEs corresponding to the highest barrier step yield an internal standard against which the relative energies of Mn^{IV}–oxyl formation and nucleophilic-attack transition states can be compared, in turn, providing indirect experimental access to these transition states. There has been a plethora of DFT studies that have focused on the O–O bond-formation reaction in O₂ evolution, but this work highlights the importance of examining the steps upstream and downstream from O–O bond formation for a comprehensive understanding of the mechanism of O₂ evolution. The ¹⁸O KIE associated with photosynthetic O₂ evolution ranges from 0.9926 to 1.0006,^{63,64} indicating that the interpretation of the PSII reaction mechanism is more complex than O–O bond formation being the rate-determining step during turnover conditions. This investigation, thus, serves as a reference point for mechanisms associated with Mn-catalyzed O–O bond formation and provides a methodology that can assist studies of the mechanism of water oxidation by the OEC during photosynthesis.

EXPERIMENTAL SECTION

Reagents. All chemicals were purchased from Sigma-Aldrich and used without further purification. Oxone (2KHSO₅·KHSO₄·K₂SO₄) was standardized using iodometric titrations.

[Mn^{III/IV}₂(μ-O)₂(terpy)₂(OH₂)₂](NO₃)₃ (**1**; where terpy = 2,2':6',2''-terpyridine) was synthesized as previously reported.²² All of the solutions were made fresh on the day of the experiment, degassed with ultrapure helium, and added to the reaction chamber by using gastight syringes. The 99.998% pure O₂ gas, used for calibration and referencing, was purchased from Matheson Gas.

Vacuum Apparatus for ¹⁸O Isotopic Experiments. A special apparatus was designed and constructed for the oxygen isotope experiments (Figure 3).

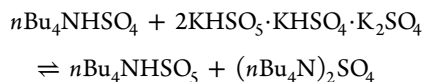
Oxygen Kinetic Isotope Effect Experiments. All ¹⁸O isotope samples (buffer, O₂ gas, and HSO₅[−]) were standardized against VSMOW (Vienna standard mean ocean water) as follows:

$$\delta(^{18}\text{O}) = \frac{(^{18}\text{O}/^{16}\text{O})_{\text{sample}}}{(^{18}\text{O}/^{16}\text{O})_{\text{VSMOW}}} - 1 \quad (5)$$

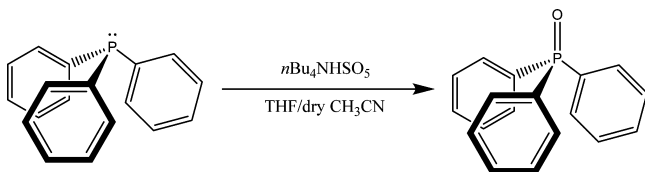
¹⁸O Composition of Buffer Solution. The oxygen isotope content of the buffer solution was analyzed by using the CO₂–H₂O equilibration method.⁴³ Acetate buffer solutions (0.23 M HOAc/OAc[−], pH 4.5) were made using either doubly deionized water or slightly enriched ¹⁸O water (made by evaporation). Aliquots of these solutions (0.3 mL) were put into Exetainer tubes that were filled with ultrahigh-purity helium and 0.3% (w/v) carbon dioxide. The solutions and the headspace CO₂ were allowed to equilibrate at 25 °C for 24 h. The CO₂ was then measured on a GasBench setup connected to a Thermo DeltaPlus XP mass spectrometer to determine ⁴⁴CO₂/⁴⁶CO₂ by a continuous-flow method.

¹⁸O Composition of Oxone. Oxone exists as the triple salt 2KHSO₅·KHSO₄·K₂SO₄, and because the isotopic composition of the reactive peroxo oxygen is needed, oxygen was transferred into another reagent for ease of oxygen isotope determination. We had previously found that the ¹⁸O isotopic abundance of the peroxo oxygen might be different from that of the other oxygen atoms²⁸ because the oxygen atoms come from different sources.⁶⁵ Potassium oxone was dissolved in deionized water with *n*Bu₄NHSO₄ and extracted with CH₂Cl₂.⁴⁴ The organic layer was dried over magnesium sulfate, and the solvent was evaporated to obtain *n*Bu₄NHSO₅. The amount of peroxymo-

nosulfate ion (HSO_3^-) extracted into the organic salt was determined by iodometric titration.



Triphenylphosphine (TPP) was mixed with $n\text{Bu}_4\text{NHSO}_3$ in a 1/1 THF/methanol solution mixture and stirred overnight at room temperature under a nitrogen atmosphere to form triphenylphosphine oxide (TPPO), which was then extracted from $n\text{Bu}_4\text{NHSO}_4$ using distilled water. This whole process was repeated three times to get an average ^{18}O isotopic composition. Triplicate runs of the reaction were also conducted using the solvent mixture of 1/1 THF/dry acetonitrile. There was an indication from labeling studies done on the oxidation of TPP by a related oxidant, persulfate ($\text{O}_3\text{SOOSO}_3^{2-}$), that there is no incorporation of the solvent oxygen atoms in the product.⁶⁵ We found that changing the solvent had no effect on the ^{18}O isotopic composition of TPPO, suggesting that the TPPO oxygen comes from HSO_3^- alone.



The reaction was performed six times, and the yields of TPPO ranged from 97% to 100%, as determined by ^{31}P NMR spectroscopy. Near 100% conversion is important to warrant that no fractionation during the reaction has taken place. The extracted TPPO was incubated in ^{18}O -enriched water for 2 weeks to examine the effect of water extraction on the isotope ratio of TPPO, and it was found that the oxygen in TPPO does not exchange with water.

The ^{18}O content of TPPO was determined by weighing the samples in Ag boats and pyrolyzing them at 1450°C in a carbon reducing environment to yield CO in a Thermo-Chemical Elemental Analyzer connected to a Thermo DeltaPlus XP mass spectrometer.⁴⁵ The carbon monoxide produced was analyzed for its ^{18}O isotopic composition. The samples were measured at Yale University and also sent to IsoForensics Lab in Salt Lake City, UT, for comparison. The largest contributor to the error of the measured isotope effect is the error associated with this reaction (both random and systematic), because our measured O_2 gas errors are 1 order of magnitude smaller.

^{18}O Composition of the Catalytic O_2 Evolved. The isotopic content of evolved O_2 was analyzed by producing and isolating the O_2 in the vacuum setup described in Figure 3. A typical run was started by injecting $50\ \mu\text{L}$ of 25 mM **1** into $950\ \mu\text{L}$ of 600 mM oxone (both solutions were made in 0.23 M HOAc/OAc^- , pH 4.5) in a well-stirred reaction chamber filled with helium. The reaction was allowed to proceed for different times corresponding to different oxone fractional conversions and stopped by quenching with 40% (w/w) KI solution. The fractional conversions used for the KIE calculation were all below 5% to prevent the effect of the water-reaction pathway on the isotopic composition of O_2 . The O_2 gas was then collected by repeated freeze–thaw cycles. The O_2 was transferred to the collection tube containing 5 Å molecular sieves at -196°C after passing it through multiple traps to purify it. The sieves were primed by heating them in a 300°C vacuum furnace for 24 h and then degassed again with a heat gun when they were loaded into the collection tube attached to the vacuum line. We ran O_2 gases of

known composition to determine if the vacuum line (traps and sieves) caused a systematic error in the observed fractionation and found that the error was negligible. The collection tubes with the sample of O_2 were then taken to a MAT 253 dual inlet mass spectrometer, and the gas was released by heat and measured in the O_2 mode against an in-house standard O_2 reference gas.^{66,67} Each sample of O_2 gas was measured eight times to determine the error. The overall error (± 0.003) associated with the KIE encompasses the error associated with the fractional conversion of oxone, the initial ^{18}O content of peroxydisulfate, and the final ^{18}O content of O_2 at each fractional conversion.

A working standard reference O_2 gas was established by calibrating it against reference CO_2 in a microanalytical vacuum line equipped with a platinized carbon reactor. The graphite and pure O_2 were combusted at 700°C to form CO_2 , which was then run on the dual-inlet mass spectrometer. The platinum ensured complete conversion of O_2 to CO_2 without any CO impurity and gave more precise isotopic composition than using graphite alone.

Deuterium Isotope Effect Experiments. The non-competitive deuterium isotope effect was determined by measuring initial rates of O_2 evolution at 25°C using a Clark-type electrode. Deuterated acetate buffer (0.23 M DOAc/OAc^- , pD 4.5) was made using 99.9% NMR grade D_2O . A $150\ \mu\text{L}$ portion of 5 mM **1** dissolved in buffer was added to 2.85 mL of 600 mM oxone solution and the initial O_2 -evolution rate recorded. The ratio [oxone]:[**1**] was kept the same as in the ^{18}O isotope effect experiments. The H/D isotope effect was calculated by taking the ratio of the average of three O_2 -evolution initial rates measured in deuterated and undeuterated buffers.

Computational Methods. Density Functional Theory. All geometries were fully optimized at the B3LYP level of density functional theory using the LanL2DZ pseudopotential basis set⁶⁸ on Mn, the 3-21G basis set on C and H atoms,⁶⁹ the 6-31G basis set on N atoms, the 6-31G(d) basis set on S atoms,^{70,71} and the 6-31+G(d) basis set on O atoms,^{72,73} along with the PCM aqueous continuum solvation model.⁴⁹ Nonanalytical integral evaluations made use of a pruned grid having 99 radial shells and 590 angular points per shell with the Gaussian 09 software package.⁷⁴ The nature of all stationary points was verified by analytic computation of vibrational frequencies, which were also used for the computation of zero-point vibrational energies and molecular partition functions and for the determination of the reactants and products associated with each transition-state structure (by following the normal modes associated with imaginary frequencies). Partition functions were used in the computation of 298 K thermal contributions to the free energy by employing the usual ideal-gas, rigid-rotator, harmonic oscillator approximation.⁷⁵ Free energy contributions were added to single-point electronic energies computed with the LanL2DZ basis set on manganese and the 6-311+G(2df,p) basis set on all other atoms to arrive at final, composite free energies. The single-point electronic energies were calculated with B3LYP with 15% Hartree–Fock exchange as suggested by a recent benchmark study.⁷⁶ Dispersion was considered with Grimme's D2 version of dispersion correction.⁵⁰

Solvation and Standard-State Corrections. Solvation effects associated with water as solvent were accounted for using the PCM continuum solvation model. The following atomic Coulomb radii were used for solute molecules: H (1.443 Å), C (1.9225 Å), N (1.83 Å), O (1.75 Å), S (2.0175 Å), and Mn (2.0 Å). A 1 M standard state was used for all species in aqueous

solution except for water itself, for which a 55.6 M standard state was employed. Thus, for all molecules but water, the free energy in aqueous solution is computed as the 1 atm gas-phase free energy, plus an adjustment for the 1 atm to 1 M standard-state concentration change of $RT \ln 24.5$, or 1.89 kcal/mol, plus the 1 M to 1 M transfer (solvation) free energy.⁷⁵ In the case of water, the 1 atm gas phase free energy is adjusted by the sum of a 1 atm to 55.6 M standard-state concentration change, or 4.27 kcal/mol, and the experimental 1 M to 1 M solvation free energy, −6.3 kcal/mol.⁷⁷

Non-Single-Determinantal State Energies. Several possible intermediates in the O₂-evolution mechanism have electronic structures that are not well described by a single determinant. In such instances, standard Kohn–Sham DFT is not directly applicable,^{75,78–80} and we adopt the Yamaguchi broken-spin-symmetry (BS) procedure^{81,82} to compute the energy of the spin-purified low-spin (LS) state as

$${}^{\text{LS}}E = \frac{{}^{\text{BS}}E({}^{\text{HS}}\langle S^2 \rangle - {}^{\text{LS}}\langle S^2 \rangle) - {}^{\text{HS}}E({}^{\text{BS}}\langle S^2 \rangle - {}^{\text{LS}}\langle S^2 \rangle)}{{}^{\text{HS}}\langle S^2 \rangle - {}^{\text{BS}}\langle S^2 \rangle} \quad (6)$$

where HS refers to the single-determinantal high-spin coupled state that is related to the low-spin state by spin flip(s) and $\langle S^2 \rangle$ is the expectation value of the total spin operator applied to the appropriate determinant. This broken-symmetry DFT approach has routinely proven effective for the prediction of state-energy splittings in metal coordination compounds.^{79,83–86}

■ ASSOCIATED CONTENT

■ Supporting Information

The Supporting Information is available free of charge on the ACS Publications website at DOI: 10.1021/acscatal.5b01976.

Complete theoretical ¹⁸O KIE methods and calculated vibrational frequencies (PDF)

■ AUTHOR INFORMATION

Corresponding Authors

*E-mail for V.S.B.: victor.batista@yale.edu.

*E-mail for G.W.B.: gary.brudvig@yale.edu.

Author Contributions

[§]These authors contributed equally to this work.

Notes

The authors declare no competing financial interest.

■ ACKNOWLEDGMENTS

The authors thank Dr. Glendon B. Hunsinger and Professor Zhengrong Wang for their immense help with mass spectrometry, Daryl Smith and Rosario Bernardo for the vacuum line construction, and Professors Hagit P. Affeck, Justine P. Roth, and Alfredo M. Angeles-Boza and Drs. Rhitankar Pal, Ivan Rivalta, and C. Moyses Araujo for helpful discussions. The experimental work was supported by the U.S. Department of Energy, Office of Science, Office of Basic Energy Sciences, Division of Chemical Sciences, Geosciences and Biosciences, grant DE-FG02-05ER15646 (G.W.B. and S.K.). V.S.B. acknowledges supercomputer time from the NESRC and financial support from the U.S. Department of Energy, Office of Science, Office of Basic Energy Sciences, Division of Chemical Sciences, Geosciences, and Biosciences, under Grant DE-SC0001423. The work at BNL (M.Z.E.) was carried out under contract DE-SC00112704 with the U.S. Department of Energy, Office of Science, Office of Basic Energy Sciences.

■ REFERENCES

- (1) Lewis, N. S.; Nocera, D. G. *Proc. Natl. Acad. Sci. U. S. A.* **2006**, *103*, 15729–15735.
- (2) Young, K. J.; Martini, L. A.; Milot, R. L.; Snoeberger, R. C., III; Batista, V. S.; Schmittenmaer, C. A.; Crabtree, R. H.; Brudvig, G. W. *Coord. Chem. Rev.* **2012**, *256*, 2503–2520.
- (3) Faunce, T.; Styring, S.; Wasielewski, M. R.; Brudvig, G. W.; Rutherford, A. W.; Messinger, J.; Lee, A. F.; Hill, C. L.; deGroot, H.; Fontecave, M.; MacFarlane, D. R.; Hankamer, B.; Nocera, D. G.; Tiede, D. M.; Dau, H.; Hillier, W.; Wang, L. Z.; Amal, R. *Energy Environ. Sci.* **2013**, *6*, 1074–1076.
- (4) Gust, D.; Moore, T. A.; Moore, A. L. *Acc. Chem. Res.* **2009**, *42*, 1890–1898.
- (5) Concepcion, J. J.; House, R. L.; Papanikolas, J. M.; Meyer, T. J. *Proc. Natl. Acad. Sci. U. S. A.* **2012**, *109*, 15560–15564.
- (6) Hohmann-Marriott, M. F.; Blankenship, R. E. *Annu. Rev. Plant Biol.* **2011**, *62*, 515–548.
- (7) Dau, H.; Zaharieva, I. *Acc. Chem. Res.* **2009**, *42*, 1861–1870.
- (8) Cox, N.; Pantazis, D. A.; Neese, F.; Lubitz, W. *Acc. Chem. Res.* **2013**, *46*, 1588–1596.
- (9) Vinyard, D. J.; Ananyev, G. M.; Dismukes, G. C. *Annu. Rev. Biochem.* **2013**, *82*, 577–606.
- (10) Vinyard, D. J.; Khan, S.; Brudvig, G. W. *Faraday Discuss.* **2015**, DOI: 10.1039/C5FD00087D.
- (11) Suga, H.; Akita, F.; Hirata, K.; Ueno, G.; Murakami, H.; Nakajima, Y.; Shimizu, T.; Yamashita, K.; Yamamoto, M.; Ago, H.; Shen, J. R. *Nature* **2015**, *517*, 99.
- (12) Armstrong, F. A. *Philos. Trans. R. Soc., B* **2008**, *363*, 1263–1270.
- (13) McEvoy, J. P.; Brudvig, G. W. *Chem. Rev.* **2006**, *106*, 4455–4483.
- (14) Cady, C. W.; Crabtree, R. H.; Brudvig, G. W. *Coord. Chem. Rev.* **2008**, *252*, 444–455.
- (15) Mullins, C. S.; Pecoraro, V. L. *Coord. Chem. Rev.* **2008**, *252*, 416–443.
- (16) Brimblecombe, R.; Dismukes, C.; Swiegers, G.; Spiccia, L. In *Molecular Solar Fuels*; Wydrzynski, T., Hillier, W., Eds.; RSC Publishing: Cambridge, United Kingdom, 2012; pp 249–272.
- (17) Singh, A.; Spiccia, L. *Coord. Chem. Rev.* **2013**, *257*, 2607–2622.
- (18) Karkas, M. D.; Verho, O.; Johnston, E. V.; Åkermark, B. *Chem. Rev.* **2014**, *114*, 11863–12001.
- (19) Kanady, J. S.; Tsui, E. Y.; Day, M. W.; Agapie, T. *Science* **2011**, *333*, 733–736.
- (20) Mukherjee, S.; Stull, J. A.; Yano, J.; Stamatatos, T. C.; Pringouri, K.; Stich, T. A.; Abboud, K. A.; Britt, R. D.; Yachandra, V. K.; Christou, G. *Proc. Natl. Acad. Sci. U. S. A.* **2012**, *109*, 2257–2262.
- (21) Zhang, C. X.; Chen, C. H.; Dong, H. X.; Shen, J. R.; Dau, H.; Zhao, J. Q. *Science* **2015**, *348*, 690–693.
- (22) Limburg, J.; Vrettos, J. S.; Liable-Sands, L. M.; Rheingold, A. L.; Crabtree, R. H.; Brudvig, G. W. *Science* **1999**, *283*, 1524–1527.
- (23) Limburg, J.; Vrettos, J. S.; Chen, H.; de Paula, J. C.; Crabtree, R. H.; Brudvig, G. W. *J. Am. Chem. Soc.* **2001**, *123*, 423–430.
- (24) Young, K. J.; Brennan, B. J.; Tagore, R.; Brudvig, G. W. *Acc. Chem. Res.* **2015**, *48*, 567–574.
- (25) Li, G.; Sproviero, E. M.; McNamara, W. R.; Snoeberger, R. C., III; Crabtree, R. H.; Brudvig, G. W.; Batista, V. S. *J. Phys. Chem. B* **2010**, *114*, 14214–14222.
- (26) Rivalta, I.; Brudvig, G. W.; Batista, V. S. *Curr. Opin. Chem. Biol.* **2012**, *16*, 11–18.
- (27) Tagore, R.; Chen, H. Y.; Crabtree, R. H.; Brudvig, G. W. *J. Am. Chem. Soc.* **2006**, *128*, 9457–9465.
- (28) Chen, H. Y.; Tagore, R.; Olack, G.; Vrettos, J. S.; Weng, T. C.; Penner-Hahn, J.; Crabtree, R. H.; Brudvig, G. W. *Inorg. Chem.* **2007**, *46*, 34–43.
- (29) Tagore, R.; Chen, H. Y.; Zhang, H.; Crabtree, R. H.; Brudvig, G. W. *Inorg. Chim. Acta* **2007**, *360*, 2983–2989.
- (30) Tagore, R.; Crabtree, R. H.; Brudvig, G. W. *Inorg. Chem.* **2008**, *47*, 1815–1823.
- (31) Cady, C. W.; Shinopoulos, K. E.; Crabtree, R. H.; Brudvig, G. W. *Dalton Trans.* **2010**, *39*, 3985–3989.

- (32) Lundberg, M.; Blomberg, M. R. A.; Siegbahn, P. E. M. *Inorg. Chem.* **2004**, *43*, 264–274.
- (33) Wang, T.; Brudvig, G.; Batista, V. S. *J. Chem. Theory Comput.* **2010**, *6*, 755–760.
- (34) Hatakeyama, M.; Nakata, H.; Wakabayashi, M.; Yokojima, S.; Nakamura, S. *J. Phys. Chem. A* **2012**, *116*, 7089–7097.
- (35) Zhou, T.; Lin, X.; Zheng, X. *J. Chem. Theory Comput.* **2013**, *9*, 1073–1080.
- (36) Rivalta, I.; Yang, K. R.; Brudvig, G. W.; Batista, V. S. *ACS Catal.* **2015**, *5*, 2384–2390.
- (37) Duan, L. L.; Bozoglian, F.; Mandal, S.; Stewart, B.; Privalov, T.; Llobet, A.; Sun, L. C. *Nat. Chem.* **2012**, *4*, 418–423.
- (38) Beckmann, K.; Uchtenhagen, H.; Berggren, G.; Anderlund, M. F.; Thapper, A.; Messinger, J.; Styring, S.; Kurz, P. *Energy Environ. Sci.* **2008**, *1*, 668–676.
- (39) Bigeleisen, J.; Wolfsberg, M. In *Advances in Chemical Physics*; Prigogine, I., Ed.; Interscience: New York, 1958; Vol. 1, pp 15–76.
- (40) Klinman, J. P.; Roth, J. P. In *Isotope Effects in Chemistry and Biology*; Kohen, A.; Limbach, H., Eds.; CRC Press: Boca Raton, FL, 2005; pp 645–670.
- (41) Parent, A. R.; Crabtree, R. H.; Brudvig, G. W. *Chem. Soc. Rev.* **2013**, *42*, 2247–2252.
- (42) Cleland, W. W. *Bioorg. Chem.* **1987**, *15*, 283–302.
- (43) Cohn, M.; Urey, H. C. *J. Am. Chem. Soc.* **1938**, *60*, 679–687.
- (44) Travis, B. R.; Ciaramitaro, B. P.; Borhan, B. *Eur. J. Org. Chem.* **2002**, *2002*, 3429–3434.
- (45) Kornel, B. E.; Gehre, M.; Hofling, R.; Werner, R. A. *Rapid Commun. Mass Spectrom.* **1999**, *13*, 1685–1693.
- (46) Northrop, D. B. *Biochemistry* **1975**, *14*, 2644–2651.
- (47) Becke, A. D. *J. Chem. Phys.* **1993**, *98*, 5648–5652.
- (48) Stephens, P. J.; Devlin, F. J.; Chabalowski, C. F.; Frisch, M. J. *J. Phys. Chem.* **1994**, *98*, 11623–11627.
- (49) Tomasi, J.; Mennucci, B.; Cammi, R. *Chem. Rev.* **2005**, *105*, 2999–3094.
- (50) Grimme, S. *J. Comput. Chem.* **2006**, *27*, 1787–1799.
- (51) Zhao, Y.; Truhlar, D. G. *J. Chem. Phys.* **2006**, *125*, 194101–194118.
- (52) Angeles-Boza, A. M.; Ertem, M. Z.; Sarma, R.; Ibanez, C. H.; Maji, S.; Llobet, A.; Cramer, C. J.; Roth, J. P. *Chem. Sci.* **2014**, *5*, 1141–1152.
- (53) Angeles-Boza, A. M.; Roth, J. P. *Inorg. Chem.* **2012**, *51*, 4722–4729.
- (54) Milikisyan, S.; Chatterjee, R.; Lakshmi, K. V. *J. Phys. Chem. B* **2011**, *115*, 12220–12229.
- (55) Roth, J. P.; Cramer, C. J. *J. Am. Chem. Soc.* **2008**, *130*, 7802–7803.
- (56) Sarma, R.; Angeles-Boza, A. M.; Brinkley, D. W.; Roth, J. P. *J. Am. Chem. Soc.* **2012**, *134*, 15371–15386.
- (57) Cook, P. F. *Enzyme Mechanism from Isotope Effects*; CRC Press: Boca Raton, FL, 1991.
- (58) Kohen, A.; Limbach, H.-H. *Isotope Effects in Chemistry and Biology*; Taylor & Francis: Boca Raton, FL, 2006.
- (59) O’Leary, M. H. *Transition States of Biochemical Processes*; Plenum Press: New York, 1978.
- (60) Stein, R. L. *J. Org. Chem.* **1981**, *46*, 3328–3330.
- (61) Ruszczycky, M. W.; Anderson, V. E. *J. Theor. Biol.* **2006**, *243*, 328–342.
- (62) Liu, F.; Concepcion, J. J.; Jurss, J. W.; Cardolaccia, T.; Templeton, J. L.; Meyer, T. J. *Inorg. Chem.* **2008**, *47*, 1727–1752.
- (63) Guy, R. D.; Fogel, M. L.; Berry, J. A. *Plant Physiol.* **1993**, *101*, 37–47.
- (64) Eisenstadt, D.; Barkan, E.; Luz, B.; Kaplan, A. *Photosynth. Res.* **2010**, *103*, 97–103.
- (65) Ball, D. L.; Edwards, J. O. *J. Am. Chem. Soc.* **1956**, *78*, 1125–1129.
- (66) Sharp, Z. D. *Am. J. Sci.* **1995**, *295*, 1058–1076.
- (67) Barkan, E.; Luz, B. *Rapid Commun. Mass Spectrom.* **2003**, *17*, 2809–2814.
- (68) Hay, P. J.; Wadt, W. R. *J. Chem. Phys.* **1985**, *82*, 299–310.
- (69) Binkley, J. S.; Pople, J. A.; Hehre, W. J. *J. Am. Chem. Soc.* **1980**, *102*, 939–947.
- (70) Franci, M. M.; Pietro, W. J.; Hehre, W. J.; Binkley, J. S.; Gordon, M. S.; DeFrees, D. J.; Pople, J. A. *J. Chem. Phys.* **1982**, *77*, 3654–3665.
- (71) Hehre, W. J.; Radom, L.; Schleyer, P. v. R.; Pople, J. A. *Ab Initio Molecular Orbital Theory*; Wiley: New York, 1986.
- (72) Hariharan, P. C.; Pople, J. A. *Theoret. chim. Acta.* **1973**, *28*, 213–222.
- (73) Clark, T.; Chandrasekhar, J.; Spitznagel, G. W.; Schleyer, P. v. R. *J. Comput. Chem.* **1983**, *4*, 294–301.
- (74) Frisch, M. J.; Trucks, G. W.; Schlegel, H. B.; Scuseria, G. E.; Robb, M. A.; Cheeseman, J. R.; Scalmani, G.; Barone, V.; Mennucci, B.; Petersson, G. A.; Nakatsuji, H.; Caricato, M.; Li, X.; Hratchian, H. P.; Izmaylov, A. F.; Bloino, J.; Zheng, G.; Sonnenberg, J. L.; Hada, M.; Ehara, M.; Toyota, K.; Fukuda, R.; Hasegawa, J.; Ishida, M.; Nakajima, T.; Honda, Y.; Kitao, O.; Nakai, H.; Vreven, T.; Montgomery, J. A.; Peralta, J. E.; Ogliaro, F.; Bearpark, M.; Heyd, J. J.; Brothers, E.; Kudin, K. N.; Staroverov, V. N.; Kobayashi, R.; Normand, J.; Raghavachari, K.; Rendell, A.; Burant, J. C.; Iyengar, S. S.; Tomasi, J.; Cossi, M.; Rega, N.; Millam, J. M.; Klene, M.; Knox, J. E.; Cross, J. B.; Bakken, V.; Adamo, C.; Jaramillo, J.; Gomperts, R.; Stratmann, R. E.; Yazyev, O.; Austin, A. J.; Cammi, R.; Pomelli, C.; Ochterski, J. W.; Martin, R. L.; Morokuma, K.; Zakrzewski, V. G.; Voth, G. A.; Salvador, P.; Dannenberg, J. J.; Dapprich, S.; Daniels, A. D.; Farkas, Ö.; Foresman, J. B.; Ortiz, J. V.; Cioslowski, J.; Fox, D. J. *Gaussian 09, Revision D.01*; Gaussian, Inc., Wallingford, CT, 2013.
- (75) Cramer, C. J. *Essentials of Computational Chemistry: Theories and Models*; 2nd ed.; Wiley: Chichester, U.K., 2004.
- (76) Siegbahn, P. E. M.; Blomberg, M. R. A. *J. Chem. Theory Comput.* **2014**, *10*, 268–272.
- (77) Camaioni, D. M.; Schwerdtfeger, C. A. *J. Phys. Chem. A* **2005**, *109*, 10795–10797.
- (78) Ziegler, T.; Rauk, A.; Baerends, E. J. *Theor. Chim. Acta* **1977**, *43*, 261–271.
- (79) Noodleman, L. *J. Chem. Phys.* **1981**, *74*, 5737–5743.
- (80) Cramer, C. J.; Truhlar, D. G. *Phys. Chem. Chem. Phys.* **2009**, *11*, 10757–10816.
- (81) Yamaguchi, K.; Jensen, F.; Dorigo, A.; Houk, K. N. *Chem. Phys. Lett.* **1988**, *149*, 537–542.
- (82) Soda, T.; Kitagawa, Y.; Onishi, T.; Takano, Y.; Shigeta, Y.; Nagao, H.; Yoshioka, Y.; Yamaguchi, K. *Chem. Phys. Lett.* **2000**, *319*, 223–230.
- (83) Noodleman, L.; Peng, C. Y.; Case, D. A.; Mouesca, J.-M. *Coord. Chem. Rev.* **1995**, *144*, 199–244.
- (84) Ciofini, I.; Daul, C. A. *Coord. Chem. Rev.* **2003**, *238–239*, 187–209.
- (85) Harvey, J. N. *Struct. Bonding (Berlin, Ger.)* **2004**, *112*, 151–183.
- (86) Neese, F. *Coord. Chem. Rev.* **2009**, *253*, 526–563.